Remote Sensing of Environment 295 (2023) 113717

Contents lists available at ScienceDirect

Remote Sensing of Environment

journal homepage: www.elsevier.com/locate/rse

Calibration of the SNPP and NOAA 20 VIIRS sensors for continuity of the MODIS climate data records

Alexei Lyapustin [a,*], Yujie Wang [b,a], Myungje Choi [b,a], Xiaoxiong Xiong [a], Amit Angal [c], Aisheng Wu [c], David R. Doelling [d], Rajendra Bhatt [d], Sujung Go [b,a], Sergey Korkin [b,a], Bryan Franz [a], Gerhardt Meister [a], Andrew M. Sayer [a,b], Miguel Roman [e], Robert E. Holz [f], Kerry Meyer [a], James Gleason [a], Robert Levy [a]

[a] NASA Goddard Space Flight Center, Greenbelt, MD, USA
[b] GESTAR II University of Maryland Baltimore County, Baltimore, MD, USA
[c] Science Systems and Applications, Inc., Lanham, MD 20709, USA
[d] NASA Langley Research Center, Hampton, VA, USA
[e] Leidos, Reston, VA, USA
[f] SSEC, University of Wisconsin–Madison, Madison, WI, USA

ARTICLE INFO

Edited by Jing M. Chen

Keywords:
MAIAC
MODIS
VIIRS
Calibration
Surface reflectance
NDVI

ABSTRACT

Accurate long-term sensor calibration and periodic re-processing to ensure consistency and continuity of atmospheric, land and ocean geophysical retrievals from space within the mission period and across different missions is a major requirement of climate data records. In this work, we applied the Multi-Angle Implementation of Atmospheric Correction (MAIAC)-based vicarious calibration technique over Libya-4 desert site to perform calibration analysis of Visible Infrared Imaging Radiometer Suite (VIIRS) on Suomi National Polar-orbiting Partnership (SNPP) and NOAA-20 satellites. For both VIIRS sensors we characterized residual linear calibration trends and cross-calibrated both sensors to MODerate resolution Imaging Spectroradiometer (MODIS) Aqua regarded as a calibration standard. The relative spectral response (RSR) differences were accounted for using the German Aerospace Center (DLR) Earth Sensing Imaging Spectrometer (DESIS) hyperspectral surface reflectance data. Our results agree with independent vicarious calibration results of both the MODIS/VIIRS Characterization Support Team as well as the CERES Imager and Geostationary Calibration Group within estimated uncertainty of 1–2%. Analysis of MAIAC geophysical products with the new calibration shows a high level of agreement of MAIAC aerosol, surface reflectance and NDVI records between MODIS and VIIRS. Excluding high aerosol optical depth (AOD), all three sensors agree in AOD with *mean difference* (*MD*) less than 0.01 and *residual mean squared difference rmsd* ~ 0.04. Spectral geometrically normalized surface reflectance agrees within *rmsd* of 0.003–0.005 in the visible and 0.01–0.012 at longer wavelengths. The residual surface reflectance differences are fully explained by differences in spectral filter functions. Finally, difference in NDVI is characterized by *rmsd* ~ 0.02 and *MD* less than 0.003 for NDVI based on VIIRS imagery bands I1/I2 and less than 0.01 for NDVI based on VIIRS radiometric bands M5/M7. In practical sense, these numbers indicate consistency and continuity in MAIAC records ensuring the smooth transition from MODIS to VIIRS.

1. Introduction

The launch of the Earth Observing System (EOS) Terra satellite in December of 1999, followed by the Aqua satellite in May 2002, started a new era in Earth Observations. The 36-channel MODerate resolution Imaging Spectroradiometer (MODIS) (Salomonson et al., 1989) is a major instrument which initiated many systematic Earth System Data Records (ESDR) (e.g., King et al., 2003; Justice et al., 1998; Esaias et al., 1998) with high quality due to both advances in the science algorithms and, importantly, due to maintenance of the high-quality calibration standards by the MODIS Characterization Support Team (MCST) with contributions from the NASA Ocean Biology Processing Group (OBPG)

* Corresponding author.
E-mail address: alexei.i.lyapustin@nasa.gov (A. Lyapustin).

https://doi.org/10.1016/j.rse.2023.113717
Received 15 April 2023; Received in revised form 6 June 2023; Accepted 8 July 2023

Table 1
VIIRS SNPP and N20 reflective bands used in this calibration study, and MODIS Aqua reference bands. Provided is spectral range, center wavelength computed as the first moment of RSR, and horizontal spatial resolution (HSR).

VIIRS Band	Range (μm)	Center Wavelength SNPP/N20 (μm)	HSR (m)	MODIS Aqua Band	Range (μm)	Center Wavelength (μm)	HSR (m)
M1	0.402–0.422	0.418/0.411	750	B8	0.405–0.420	0.412	1000
M2	0.436–0.454	0.445/0.446	750	B3	0.459–0.479	0.466	500
M3	0.478–0.498	0.489/0.489	750	B3	0.459–0.479	0.466	500
M4	0.545–0.565	0.551/0.557	750	B4	0.545–0.565	0.554	500
I1	0.600–0.680	0.638/0.643	375	B1	0.620–0.670	0.646	250
M5	0.662–0.682	0.671/0.668	750	B1	0.620–0.670	0.646	250
I2	0.846–0.885	0.861/0.867	375	B2	0.841–0.876	0.856	250
M7	0.846–0.885	0.861/0.868	750	B2	0.841–0.876	0.856	250
M8	1.230–1.250	1.241/1.241	750	B5	1.230–1.250	1.242	500
I3/M10	1.580–1.640	(I3) 1.601/1.604	375	B6	1.628–1.652	1.629	500
		(M10) 1.602/1.605	750				
M11	2.225–2.275	2.257/2.259	750	B7	2.105–2.155	2.114	500

and other science teams. This combination of science product quality and accurate and stable long-term calibration of the MODIS instruments created the basis for the NASA Climate Data Records (CDRs) used for monitoring and evolving our understanding of the Earth System functioning and its change in time.

MODIS calibration in the visible – shortwave infrared (SWIR) spectral region (0.412–2.13 μm) relies on the solar diffuser (SD), SD stability monitor (SDSM), periodic moon observations through roll maneuvers along with increasing reliance on monitoring of the quasi-stable desert calibration sites to maintain the long-term stability of calibration (e.g., Xiong et al., 2003; Sun et al., 2014; Angal et al., 2020). A comprehensive and detailed overview of the MCST calibration procedures can be found in Xiong et al. (2020). While continuous MCST work helps identify, explain and correct for major changes in MODIS calibration over its 20+ year-long history, analysis of patterns and trends in the derived geophysical products often provides a better sensitivity to the details of MODIS calibration and its changes over time. For instance, the OBPG's seasonal analysis of derived chlorophyl-a concentrations over ocean from MODIS Terra in comparison to MODIS Aqua led to development of the polarization correction algorithm of the MODIS-Terra L1B data (Kwiatkowska et al., 2008; Meister et al., 2012). On the other hand, a long-term analysis of the spectral surface reflectance over several CEOS (Committee on Earth Observation Satellites) desert sites generated by the Multi-Angle Implementation of Atmospheric Correction (MAIAC) algorithm (Lyapustin et al., 2018) provided residual de-trending of both MODIS sensors and cross calibration of MODIS Terra to the much more stable and predictable MODIS Aqua (Lyapustin et al., 2014). While MODIS L1B data is reported without these corrections, which are often discipline-specific, the aforementioned polarization correction of MODIS Terra along with residual de-trending of the two sensors and Terra-to-Aqua cross-calibration have been implemented in the MODIS land discipline processing since Collection 6 (C6) to maintain high accuracy standards. The ability to treat two MODIS sensors as one due to advanced calibration is very beneficial to algorithms based on time series analysis and requiring a high frequency of observations, like MAIAC. Removal of the long-term calibration trends gains a particular importance for the climate change analyses based on the long-term bio/geophysical satellite records.

As MODIS nears its end of mission operation, NOAA's Visible Infrared Imaging Radiometer Suite (VIIRS) instrument steps into the forefront to gradually replace MODIS for the Earth observations at a coarse resolution. At present, there are three VIIRS instruments in space: Suomi National Polar-orbiting Partnership (SNPP) was launched in 2011, NOAA 20 (N20) satellite has been operating since 2017, and NOAA 21 launched in 2022 has recently become operational. The 22-channel VIIRS sensor in many regards is similar to MODIS and is manufactured by the same vendor. In addition to a day and night band, VIIRS has 16 radiometric and 5 imagery bands with nadir resolution of 750 m and 375 m, respectively, while MODIS has 2 bands at 250 m, 5 bands at 500 m, and the remaining bands at 1 km nadir resolution (see Table 1 for select VIIRS and MODIS reflective bands). At the same time, VIIRS provides a constrained growth of footprint with scan angle, about a factor of 2 at the edge-of-scan, compared to MODIS' growth by a factor of 8. Due to its wider swath of 3000 km, the single VIIRS sensor provides a daily global coverage of the Earth, while MODIS at 2330 km swath has near-daily coverage with gaps near the equator. The wider swath of VIIRS is achieved via a wider range of scan angles which translates to a maximum view zenith angle (VZA) of VIIRS ~72° versus ~62° from MODIS accounting for the Earth's curvature.

To become a MODIS successor and extend MODIS ESDRs, VIIRS should agree with MODIS in absolute calibration. However, the accumulated body of the VIIRS SNPP and N20 calibration characterization indicates that the SNPP VIIRS is generally calibrated higher and VIIRS on NOAA 20 is calibrated lower than MODIS, while the difference between the two VIIRS sensors can be as high as 5–7% (e.g. Eplee et al., 2015; Sayer et al., 2017; Wu et al., 2020; Xiong et al., 2020; Meyer et al., 2020).

Because VIIRS is part of the NOAA's Joint Polar Satellite System (JPSS), NOAA supports VIIRS calibration (e.g., Choi et al., 2020) as well as science processing through its Comprehensive Large Array-data Stewardship (CLASS) system (Zhou et al., 2019). Here, we focus on the separate NASA processing of the VIIRS data, where VIIRS L1B calibration is provided by the NASA VIIRS Characterization Support Team (VCST) (Xiong et al., 2020; Twedt et al., 2022). In this work, we further develop the MAIAC-based desert calibration technique (Lyapustin et al., 2014) and apply it to characterize residual VIIRS trends and cross-calibrate both VIIRS sensors to MODIS Aqua. This paper is structured as follows: Section 2 describes VIIRS de-trending analysis. VIIRS-MODIS cross-calibration study is covered in section 3. This section also provides a compendium of vicarious calibration results from different methods obtained by different teams. Section 4 gives a science assessment of the derived VIIRS calibration based on analysis of MAIAC aerosol and surface reflectance products. The main results of this study are summarized in Conclusions.

2. VIIRS trend analysis

Table 1 lists reflective VIIRS and MODIS channels which are the focus of this work. This table omits the unique VIIRS day and night (DNB) band as well as VIIRS band M6 (0.739–0.754 μm) which cannot be used over bright desert due to saturation as well as the MODIS 1 km resolution "ocean" channels 9–16. The provided band center wavelengths are computed as a first moment of the relative spectral response (RSR) functions.

We are using the latest L1B calibration for satellite datasets: Collection 6.1 with polarization correction, based on pre-launch characterization, and de-trending for MODIS Aqua (note that MODIS Terra, not used in this study, has additional polarization correction and cross-calibration to MODIS Aqua), VIIRS SNPP C2.0, and VIIRS N20 C2.1. L1B data for the 1200 km tile covering the Libya desert were provided by the

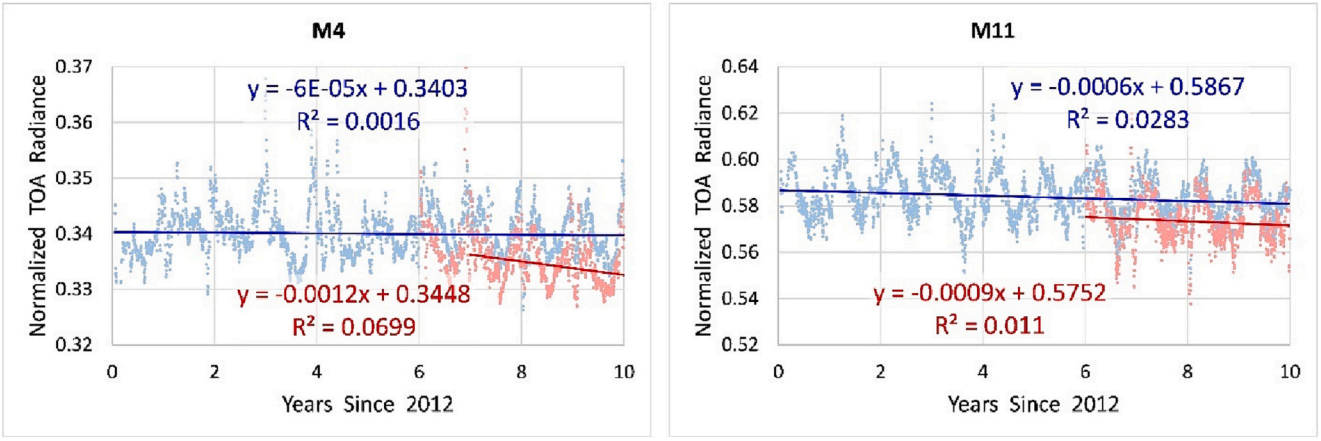

Fig. 1. An example of trend analysis for the VIIRS SNPP (blue) and N20 (red) bands M4 and M11. (For interpretation of the references to colour in this figure legend, the reader is referred to the web version of this article.)

MODIS Adaptive Processing System (MODAPS). Below, MODIS or MODIS-A will stand for MODIS Aqua.

This work uses Libya-4 desert calibration site (28.55°N, 23.39°E). It is one of several quasi-stable desert sites recommended by CEOS based on several criteria including the long-term stability related to very low annual rainfall, spatial homogeneity at scales of several km, high surface reflectance and low average aerosol loading. Lyapustin et al. (2014) analyzed seven different CEOS-recommended sites and excluded three (Niger, Sudan-1, Mali-1) as not reliable for calibration analysis. The remaining four sites (Libya-1, Libya-2, Libya-4, Egypt-1) produce very similar calibration results well represented by Libya-4.

The trend analysis is based on the MODIS and VIIRS data processing by the MAIAC algorithm. We are using the latest MAIAC Collection 6.1 (C6.1) algorithm which for the selected desert calibration site (Libya-4) is equivalent to C6 algorithm described in Lyapustin et al. (2018). MAIAC is a multi-disciplinary algorithm providing a suite of atmospheric, land surface, snow and coastal ocean properties. For this work, we are using MAIAC cloud/cloud shadow mask, aerosol optical depth (AOD), column water vapor (from MODIS-A), land surface bidirectional reflectance factors (BRF) often called 'surface reflectance' (SR), and bidirectional reflectance distribution function (BRDF) model parameters. In operational processing, these properties are generated at 1 km resolution on a global Sinusoidal grid for MODIS and will be generated at 750 m resolution for VIIRS (375 m for the imagery bands). For this work, we "over-grid" MODIS 500 m bands 1–7, and 1 km band 8 to the VIIRS 750 m grid. As the final analysis is done at 5 × 5 and 10 × 10 pixel aggregation for the VIIRS radiometric and imagery bands, respectively, centered at the Libya-4 site and representing an area of about 4 × 4 km^2, the possible oversampling does not affect the final result.

The trend analysis consists of several steps:

1) Perform MAIAC processing of the full overlapping record of MODIS-A and SNPP and N20 VIIRS data (since 2011). Because VIIRS lacks the water vapor near-infrared (NIR) channel at 0.94 μm for the high-resolution column water vapor (CWV) retrieval, for VIIRS processing we are using the National Center for Environmental Predictions Global Data Assimilation System (NCEP GDAS) ancillary CWV at 1° resolution interpolated to the MAIAC grid. Similarly, the ancillary NCEP ozone data is used for ozone correction.
2) Variations in the sensor view geometry create significant variability at the top of atmosphere, which is a source of high noise for the calibration analysis. To reduce this noise, at the second step we are using sensor-specific MAIAC retrieval results (e.g., AOD, BRDF) to simulate the top-of-atmosphere (TOA) reflectance for the normalized view geometry of SZA = 30° and nadir view for each 750 m grid cell. Such geometric normalization reduces variability of reflectance at the bottom of atmosphere by a factor of 2–5 (e.g., Lyapustin et al., 2012). At the TOA, normalization additionally mitigates variability by constraining signal of the atmospheric backscattering (or path reflectance).
3) The generated multi-year time series of normalized TOA reflectance is analyzed for the linear calibration trend with assessment of its significance using Student's *t*-test at 0.05 significance level. Here, we only test for a long-term linear calibration trend as the MCST/VCST calibration procedures capture the higher-magnitude short-term sensor calibration variations (e.g., Eplee et al., 2015; Xiong et al., 2020; Mu et al., 2020; Twedt et al., 2022).

Table 2
Results from trend analysis of SNPP and N20 VIIRS including slope and intercept of linear regression, and ratio slope/Intercept in units of reflectance (change)/unit reflectance/year.

Band	Intercept		Slope		Slope/Intercept (Trend/year/unit of refl.)	
	SNPP	N20	SNPP (× 10^{-3})	N20 (× 10^{-3})	SNPP	N20
M1	0.224	0.209	−0.016 ± 0.027	−1.12 ± 0.16/−0.8	−7.16E-05	−5.35E-03
M2	0.230	0.219	−0.13 ± 0.033	−0.98 ± 0.15/−1.3	−5.55E-04	−4.47E-03
M3	0.251	0.240	−0.055 ± 0.027	−0.98 ± 0.12/−2	−2.20E-04	−4.08E-03
M4	0.340	0.336	−0.063 ± 0.029	−1.24 ± 0.15/−1.4	−1.84E-04	−3.67E-03
M5	0.499	0.476	−0.073 ± 0.034	−0.53 ± 0.17/−0.7	−1.47E-04	−1.11E-03
M7	0.586	0.565	−0.31 ± 0.043	−0.26 ± 0.22/−0.8	−5.31E-04	−4.64E-04
M8	0.662	0.645	−0.44 ± 0.052	−0.11 ± 0.28/0.9	−6.57E-04	−1.74E-04
M10	0.696	0.681	−0.39 ± 0.046	0.81 ± 0.29/0.0	−5.61E-04	1.19E-03
M11	0.587	0.576	−0.59 ± 0.063	−1.49 ± 0.35	−1.00E-03	−2.59E-03
I1	0.463	0.451	−0.31 ± 0.071	−0.82 ± 0.28/−1.5	−6.70E-04	−1.83E-03
I2	0.585	0.563	−0.37 ± 0.070	0.004 ± 0.26/−0.5	−6.28E-04	7.03E-06
I3	0.706	0.670	−0.59 ± 0.085	0.71 ± 0.30/~0.0	−8.43E-04	1.07E-03

Fig. 1 gives an example of trends for the VIIRS bands M4 and M11. The first 12–18 months of VIIRS N20 band M4 (as well as M1-M3), show notably higher values of normalized TOA radiance compared to later

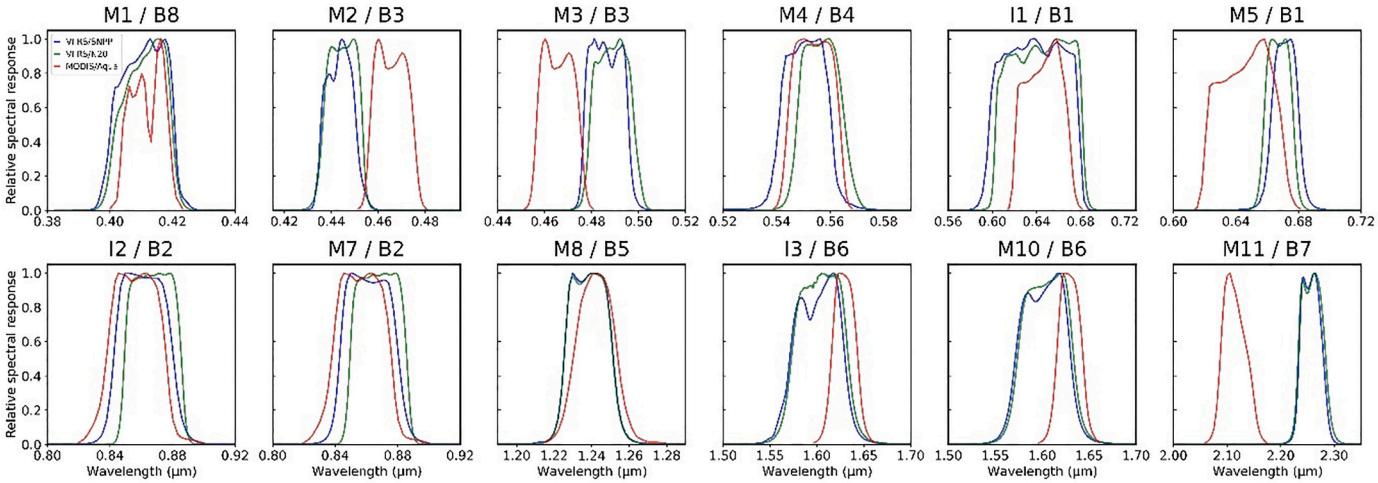

Fig. 2. Relative Spectral Response (RSR) functions of MODIS Aqua and VIIRS SNPP and N20. (For interpretation of the references to colour in this figure legend, the reader is referred to the web version of this article.)

years. For this reason, we excluded the first year from the trend analysis the results of which are given in Table 2 for both SNPP and N20 VIIRS.

All bands for both sensors show negative trends. The main result is reported in the 5th column (Slope/Intercept) of Table 2 with the units of Reflectance (change) per unit reflectance per year. For instance, for band M8 (1.24 μm) of SNPP, the reduction of TOA reflectance (R) at $R = 0.5$ over 10 years is −6.57E-04*0.5*10 = −0.0033, or about −0.3%.

In the "Slope" columns of Table 2 we also show the VIIRS N20 trend derived by VCST over Libya-4 (Fig. 9 from Twedt et al., 2022) as a second value separated by '/'. VCST reported a preliminary trend for a single fixed scan angle at 83 km from nadir using a much larger averaging area of 32 × 32 pixels. In addition, seasonal variations are removed by matching the TOA reflectance using Roujean et al. (1992) BRDF model whereas MAIAC uses Ross-Thick Li-Sparse BRDF model (Lucht et al., 2000) derived from atmospherically corrected surface reflectance. In addition to M6, MCST also excluded band M11 from the analysis. Despite methodological differences and the preliminary nature of VCST data, we agree on the sign of the trend in bands M1-M7 and I1. The magnitude of trends is within 0.3×10^{-3} in M1-M2, M4-M5 and within $(0.5–1) \times 10^{-3}$ in other channels, indicating a good general agreement given the relatively large uncertainties because of the short mission period.

Owing to a decade-long record of measurements, the VIIRS SNPP trends were recently characterized for individual detectors by VCST using deep convective clouds and deserts (Mu et al., 2020) to mitigate striping while the general long-term trends were removed in C2.0 L1B data earlier (Lei et al., 2015). This explains why, except for bands M7-M8, our residual trends for VIIRS SNPP are significantly lower than those found for VIIRS N20.

3. VIIRS cross-calibration to MODIS aqua

The trend analysis described above is a well-established technique which we used since 2013 to periodically update MODIS Terra and Aqua calibration following updates in MCST calibration algorithm and in OBPG polarization coefficients. The de-trended data allow to derive cross-calibration, or gain adjustment, factors within the same "family" of instruments, e.g., MODIS on Terra and Aqua, or VIIRS on SNPP and N20 as they have close RSRs. Effectively, the ratio of offsets between SNPP and N20 VIIRS gives the gain adjustment to ensure calibration consistency.

Such approach is no longer valid when RSRs of the instruments are different, as in case of MODIS and VIIRS. Fig. 2 shows the respective RSRs of MODIS Aqua and VIIRS SNPP and N20 sensors in the visible-

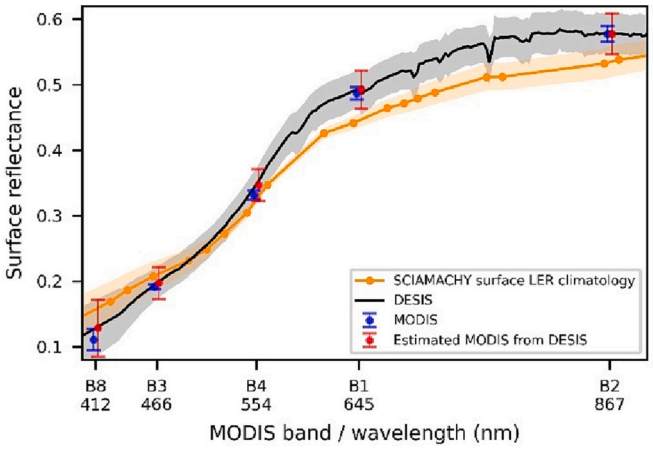

Fig. 3. Spectral LER of DESIS and SCIAMACHY. Red dots show the convolved DESIS LER to estimate MODIS reflectance, and blue dots show spectral BRF calculated from MAIAC MODIS BRDF. (For interpretation of the references to colour in this figure legend, the reader is referred to the web version of this article.)

near IR and in shortwave IR (SWIR). The difference in RSR and effective band center wavelength causes a spectral shift in both surface reflectance and atmospheric backscattering signals at TOA. This shift is traditionally accounted for by using spectral band adjustment factor (SBAF), e.g. from NASA-LaRC (Scarino et al., 2016) based on the SCanning Imaging Absorption SpectroMeter for Atmospheric CHartographY (SCIAMACHY) data (Bovensmann et al., 1999). Here, we are using German Aerospace Center (DLR) Earth Sensing Imaging Spectrometer (DESIS) flying on board the International Space Station (ISS) since 2018. DESIS is a hyperspectral imager measuring spectral radiance reflected by Earth from 400 nm to 1000 nm with spectral sampling of 2.55 nm and a full width of half maximum (FWHM) of about 3.5 nm, total of 235 channels (Krutz et al., 2019; Alonso et al., 2019). The spatial resolution is 30 m with 1024 pixels across-track and ~ 30 km swath.

By our request, DESIS has been collecting spectra over Libya-4 site since 2019 which translates to 97 presently accumulated granules. The Libya-4 region of interest is centered at 28.55°N and 23.39°E. To avoid uncertainties of geolocation and to test the effect of the averaging area, we are using the 3×3 km^2 and 6×6 km^2 aggregated areas for our analysis. Comparison of 3 km and 6 km boxes showed no difference in the results. Since individual DESIS granules sometimes have stray light

Table 3
Spectral Band Adjustment Factor (SBAF) for SNPP and N20 VIIRS to MODIS Aqua, and pair-wise cross-calibration coefficients among the three sensors.

Band	SBAF		X-calibration Coefficients		
	Aqua/SNPP	Aqua/N20	Aqua/SNPP	Aqua/N20	SNPP/N20
B8/M1	0.960	1.001	0.9738 ± 0.033	1.0277 ± 0.034	1.0554 ± 0.028
B3/M2	1.197	1.191	0.9516 ± 0.031	1.0137 ± 0.026	1.0653 ± 0.034
B3/M3	0.889	0.882	0.9818 ± 0.023	1.0290 ± 0.021	1.0481 ± 0.021
B4/M4	1.026	0.978	0.9827 ± 0.018	1.0367 ± 0.018	1.0550 ± 0.018
B1/M5	0.959	0.962	0.9780 ± 0.017	1.0212 ± 0.017	1.0442 ± 0.016
B2/M7	1.001	0.999	0.9707 ± 0.017	1.0083 ± 0.017	1.0387 ± 0.017
M8	–	–	–	–	1.0264 ± 0.017
M10	–	–	–	–	1.0215 ± 0.016
M11	–	–	–	–	1.0198 ± 0.040
B1/I1	1.016	1.004	0.9917 ± 0.023	1.0316 ± 0.021	1.0402 ± 0.026
B2/I2	1.001	0.998	0.9726 ± 0.018	1.0131 ± 0.018	1.0416 ± 0.019
I3	–	–	–	–	1.0540 ± 0.018

features near the edges of swath and sometimes contain bad quality pixel lines in the middle of the scene, we manually selected a total of twelve good quality scenes from Jan. 2019 to Aug. 2021 for our analysis representing DESIS L2A atmospherically corrected surface reflectance version 2.13 dataset. Most observations were collected at view angles within 3–24° and at high solar zenith angle (53–65°). Because DESIS data sometimes exhibit spectral noise, the climatological SCIAMACHY surface Lambertian-equivalent reflectivity (LER) was used to smooth DESIS spectra (Tilstra et al., 2017).

An example of the DESIS smoothed spectra for 3×3 km^2 aggregated area and of the much coarser resolution SCIAMACHY LER at $1^\circ \times 1^\circ$ centered at Libya-4 is shown in Fig. 3. The shaded area represents ± one standard deviation over 12 acquisitions and related monthly SCIAMACHY dataset (https://www.temis.nl/surface/albedo/scia_ler.php) (Tilstra et al., 2017). The difference in the DESIS and SCIAMACHY spectra may be partly due to a coarse resolution of SCIAMACHY, ~105 km, though we cannot exclude calibration difference. The blue dots show MAIAC MODIS Aqua spectral BRF calculated from MAIAC BRDF MCD19A2 product (Lyapustin et al., 2018) where error bars represent standard deviation from 12 days of DESIS acquisitions. Both MODIS and DESIS measurements are normalized to nadir view and SZA = 30°. DESIS convolved with MODIS RSR is displayed by the red dots, spectrally shifted for convenience. Such a close MODIS-DESIS agreement implies that we can use DESIS spectra to derive VIIRS-to-MODIS SBAFs to account for the RSR differences.

The DESIS spectral LER (ρ_λ) was convolved to MODIS Aqua and SNPP and N20 VIIRS spectral bands using the respective RSRs and solar irradiance (E_λ) as follows:

$$\rho_{simulated} = \frac{\int_0^\infty \rho_\lambda E_{s,\lambda} RSR_\lambda d\lambda}{\int_0^\infty E_{s,\lambda} RSR_\lambda d\lambda} \simeq \frac{\int_0^\infty \rho_\lambda E_\lambda RSR_\lambda d\lambda}{\int_0^\infty E_\lambda RSR_\lambda d\lambda}. \quad (1)$$

Above, $E_{s,\lambda}$ and E_λ are spectral irradiance at the bottom and top of atmosphere respectively. Because MODIS and VIIRS spectral bands are relatively narrow (~10 nm) and typical aerosol optical depth over Libya desert is low (see Fig. 5), the substitution of the surface irradiance with the TOA irradiance still gives a highly accurate result, within several percent at 0.412 μm where the atmospheric effects are largest, with accuracy increasing with wavelength along with the reduction of the total optical depth and decrease in atmospheric scattering. We used the "NRLSSI2" solar irradiance model (Coddington et al., 2016) and trapezoidal rule for the integral. It should be mentioned that while the use of approximation (1) is justified for MODIS and VIIRS due to their narrow bands, an accurate expression using the surface spectral irradiance should be used when spectral bands are wide.

The average SBAFs for reflective bands of VIIRS sensors relative to MODIS Aqua, in other words surface reflectance ratios, over Libya-4 site are presented in Table 3.

With SBAFs generated, the VIIRS to MODIS Aqua cross-calibration coefficients are calculated as follows:

1) VIIRS BRDFs, generated by MAIAC at VIIRS wavelengths (λ), are spectrally adjusted to the MODIS Aqua reference wavelengths (λ_1), $\rho_{\lambda 1}^{VIIRS} = \rho_\lambda^{VIIRS} SBAF(\lambda, \lambda_1)$.
2) Using adjusted VIIRS BRDF and retrieved MAIAC VIIRS AOD, we recompute VIIRS TOA reflectance for the normalized view geometry, but at MODIS-A wavelengths λ_1. In this case, both surface and atmospheric contributions from VIIRS are adjusted to the MODIS-A reference wavelength, so MODIS and VIIRS TOA data are directly comparable.
3) The ratio of de-trended spectrally adjusted VIIRS and MODIS TOA reflectance at normalized view geometry gives the gain adjustment factors for the VIIRS sensors.

Fig. 4 shows the combined result of de-trending and spectral adjustment of VIIRS in bands M1-M5, M7, and I1, I2. VIIRS SNPP is always higher than both MODIS-A and VIIRS N20. The N20 VIIRS is relatively close than MODIS-A but lower.

There is a residual seasonality at the level of ~0.01–0.03. Physically, it is caused by the seasonal changes in the solar elevation and variations in surface topography, including sand dunes and their shadows clearly visible in the high resolution DESIS images. The residual seasonal pattern is consistent in the visible range for both MODIS-A and VIIRS with higher values in December–January (highest SZA). The exception is MODIS-A band 8 (0.412 μm) which exhibits the opposite pattern. The reason for such a difference is presently not understood. The current L1B calibration procedure for MODIS Aqua uses pre-launch polarization sensitivity characterization and does not account for a possible change post-launch. Removing polarization correction in MODIS-A band 8 resulted in negligible change. Whatever the cause, this different behavior of MODIS band 8 may affect our gain analysis for VIIRS channel M1.

Results of the cross-calibration are summarized in Table 3 which also gives SBAFs for the SNPP and N20 VIIRS. It's important to emphasize that SBAFs were derived for the Libya-4 site and do not translate to other locations unless the surface has similar SR spectrum. The gain adjustment coefficients for SNPP and N20 to match MODIS-A are only given for bands M1-M5, M7 and I1-I2, which fall within DESIS spectral range of 0.4–1 μm. At longer wavelengths, we assume the better calibrated NOAA 20 as a reference and apply gain adjustment to SNPP VIIRS. The VIIRS NOAA 20 calibration is close to that of MODIS-A and systematically lower by 1–3% on average. The SNPP VIIRS is systematically higher than MODIS Aqua by 2–5% on average.

As a quick check, Fig. 5 shows monthly-average MAIAC AOD at 0.55 μm over Libya-4 before and after applying calibration to VIIRS SNPP and NOAA 20. At original calibration (left), AOD from SNPP VIIRS was overestimated while N20 VIIRS and MODIS-A were in a good agreement. After calibration (right), all three sensors show good agreement.

It is important to compare our results with calibration analysis of other leading groups. Table 4 provides a summary of the comparative analysis of the radiometric biases (in percentage) between the MODIS and VIIRS analogous channels derived from this study with those from MCST/VCST at GSFC and the CERES Imager and Geostationary

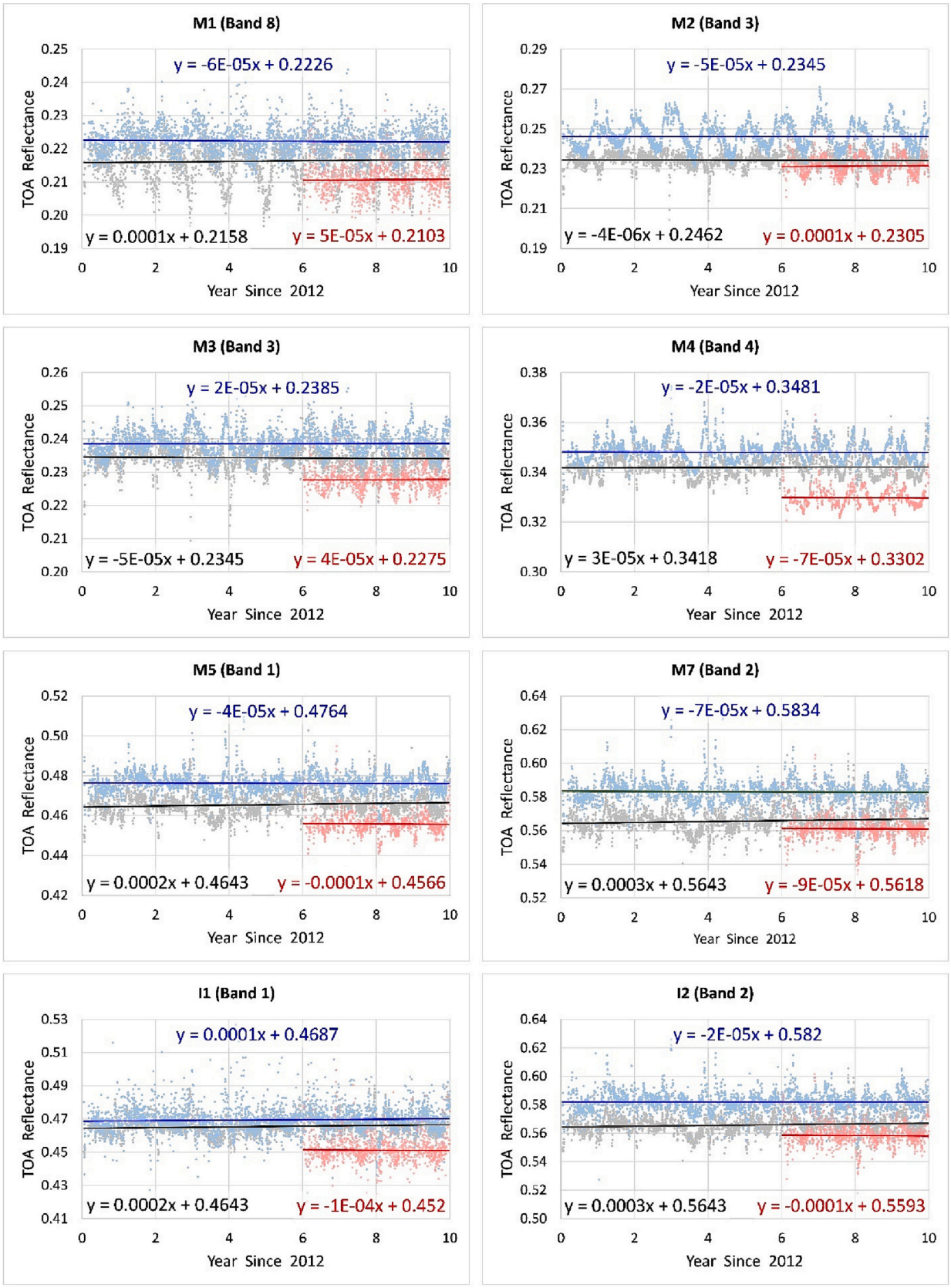

Fig. 4. Final de-trended MODIS Aqua (black) and spectrally adjusted VIIRS SNPP (blue) and N20 (red) geometrically normalized TOA reflectance for VIIRS bands M1-M5, M7 and I1, I2. (For interpretation of the references to colour in this figure legend, the reader is referred to the web version of this article.)

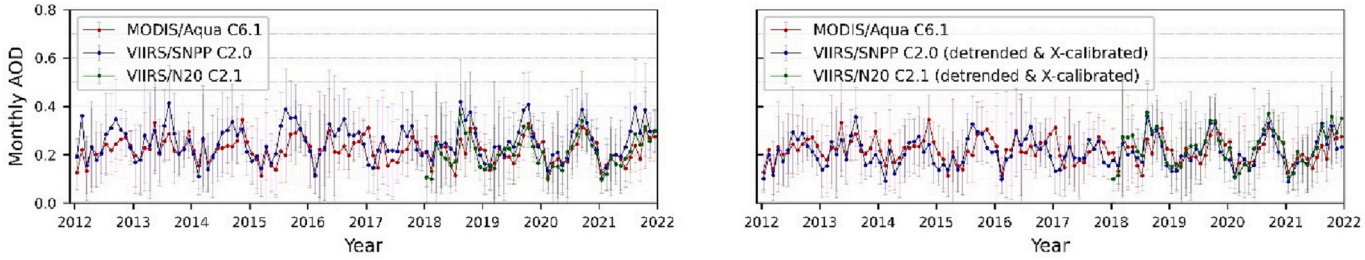

Fig. 5. Monthly-average MAIAC AOD at 0.55 μm over Libya-4 before (left) and after (right) applying calibration to VIIRS SNPP and NOAA 20. The error bars show the standard deviation.

Table 4
Cross-calibration biases (%) among MODIS Aqua (A), VIIRS SNPP (S) and VIIRS N20 (N) from different sources. A negative A/S bias means SNPP-VIIRS is brighter than Aqua-MODIS, and vice-versa. The first column gives the reference MODIS band (B) used to calibrate the VIIRS (M or I) band. An italics font indicates a different MODIS reference band used in analysis.

Band Pair	This work			MCST/VCST (Wu et al., 2022)			CERES-IGCG (LaRC)			Meyer et al. (2020)		Sayer et al. (2017)
	A/S	A/N	S/N	A/S	A/N	S/N	A/S	A/N	S/N	A/S	A/N	A/S
B8/M1	−2.6	2.8	5.5	−5.0–3.8	2.6–4.8	5.9–7.9	–	–	–	–	–	−0.5
B3/M2	−4.8	1.4	6.5	*B9: −0.5–1.5*	*5.4–6.2*	5.8–6.6	–	–	–	–	–	*B9: 0*
B3/M3	−1.8	2.9	4.8	*B10: −5.5–3.2*	*−1.1-1.7*	4.4–5.2	−1.8	3.7	5.6 ± 0.2	–	–	−0.8
B4/M4	−1.7	3.7	5.5	−0.3–2.6	1.9–3.6	3.4–5.5	−2.8	2.9	5.8 ± 0.2	–	–	−4.4
B1/M5	−2.2	2.1	4.4	−2.0–0.6	2.4–6.0	3.4–5.4	−3.1	2.4	5.4 ± 0.2	−5.0	0	−5.9
B2/M7	−2.9	0.8	3.8	−1.1–0.0	0.7–3.1	2.5–4.0	−2.1	2.3	4.2 ± 0.2	−3.0	1.0	−4.0
B5/M8	–	–	2.6	−3.4–1.9	−1.4-0.5	1.8–2.9	−3.1	−1.0	2.0 ± 0.2	−1.0	2.0	1.0
B6/M10	–	–	2.2	−3.5–1.3	–	1.2–2.9	−1.5	1.4	2.5 ± 0.3	−2.0	2.0	−2.0
B7/M11	–	–	2.0	–	–	1.2–2.1	–	–	1.6 ± 0.5	−3.0	−1.0	−7.0
B1/I1	−0.8	3.2	4.0	−0.6–1.3	2.7–4.2	3.0–4.8	−1.0	3.8	4.8 ± 0.2	–	–	–
B2/I2	−2.7	1.3	4.2	−1.0–0.1	1.1–3.0	2.6–3.1	–	–	–	–	–	–
B6/I3	–	–	5.4	−3.5–1.8	−0.3-2.1	3.1–3.9	−2.2	2.4	5.0 ± 0.3	–	–	–

Calibration Group (CERES-IGCG) at NASA Langley Research Center (LaRC).

The latest MCST/VCST results (Wu et al., 2022) combine data from four different vicarious calibration techniques including simultaneous nadir overpass (SNO, e.g., Cao et al., 2004; Chu et al., 2018), analysis over desert sites including Libya-4 (e.g., Wu et al., 2012) and Antarctica Dome C ice/snow site (Dome C, Uprety and Cao, 2015), and the Deep Convective Cloud (DCC) method (Doelling et al., 2015; Mu et al., 2017). Overall, four different techniques produce close results generally within 1–2%. For SNPP/N20, MAIAC-based results are within the range of MCST/VCST values for bands M2-M8 and I1, 0.4% lower for M1 and 1.1% and 1.5% higher for I2 and I3, respectively. For Aqua/N20 and Aqua/SNPP, our results agree within 0.3% and 1.8%, respectively, except for bands M2-M3 where comparison cannot be made because selected MODIS reference bands were different. In summary, this comparison of independent techniques shows an agreement well within our uncertainty estimates of about ±(1–2)%.

The NASA-Langley CERES-IGCG employs three independent SNPP to NOAA-20 VIIRS intercalibration approaches: two pseudo invariant calibration target approaches utilizing tropical DCC (Doelling et al., 2011; Doelling et al., 2013; Bhatt et al., 2020) and the Libya-4 desert site (Doelling et al., 2022a, 2022b) as well as all-sky tropical ocean ray-matching (Haney et al., 2022; Doelling et al., 2022a, 2022b) employing Aqua-MODIS as a transfer radiometer. Spectral band adjustments for MODIS and VIIRS reflective solar bands are based on SCIAMACHY hyper-spectral radiances (Scarino et al., 2016), except for M11, for which the SBAF was computed using the Hyperion data over the inter-calibration targets. The cross-calibration analysis was conducted in reflectance scale to avoid any potential impact of differences between the solar irradiance models used by the MODIS and two VIIRS sensors in their ground processing systems (Bhatt et al., 2021). The three approaches were consistent within 0.8%, except for band M10 which agrees within 1.4%. The biases from the three approaches were aggregated using an inverse-variance weighting method to minimize the variance of the weighted average. The SNPP and NOAA-20 VIIRS biases relative to Aqua-MODIS are based on the ray-matching approach with uncertainties mostly within 0.8%. Note that the B2/M7 MODIS and VIIRS biases have uncertainties of 1.3%, since the MODIS B2 channel saturates over bright clouds. The channel comparison results are shown in Table 4 under CERES-IGCG (LaRC).

The MAIAC SNPP/N20 VIIRS biases were within −1.0% to +0.6% of the CERES-IGCG results, where the CERES-IGCG biases were mostly larger except for bands M8 and I3. The CERES-IGCG Libya-4 SNPP/N20 VIIRS biases were lower than the combined approach on average by ~0.5% for wavelengths less than 1 μm. The relative biases computed between Aqua-MODIS and two VIIRS analogous channels by MAIAC and CERES-IGCG are within 1%, except for M7, which differed by 1.4%, for which the CERES ray-matching approach may be impacted by bright cloud saturation in the corresponding MODIS band 2.

Two other approaches, shown last in Table 4, have been developed and applied by individual science algorithm groups. Sayer et al. (2017) used simultaneous MODIS-A/SNPP VIIRS overpasses over dark water scenes with closely matched geometry to cross-calibrate VIIRS to MODIS, accounting for spectral response function differences. Meyer et al. (2020) used the same geometric matchup protocol except focused on bright, low-level liquid water cloud pixels. These independent analyses, together sampling the gamut of dark to bright pixels, also tend to agree with one another and the other results within Table 4 to within the ~1–4% level. Notably, the techniques generally agree about the spectral shape of the correction factors. The largest disagreements in magnitude tend to be in the SWIR, where the radiative transfer is more complicated due to the impact of potential uncertainties in gas transmittances, refractive index of liquid water clouds (Meyer et al., 2020), and inherent uncertainties in ratios of small numbers (Sayer et al., 2017). A shorter time record and use of the earlier C1.1 L1B calibration for SNPP VIIRS may also contribute some difference.

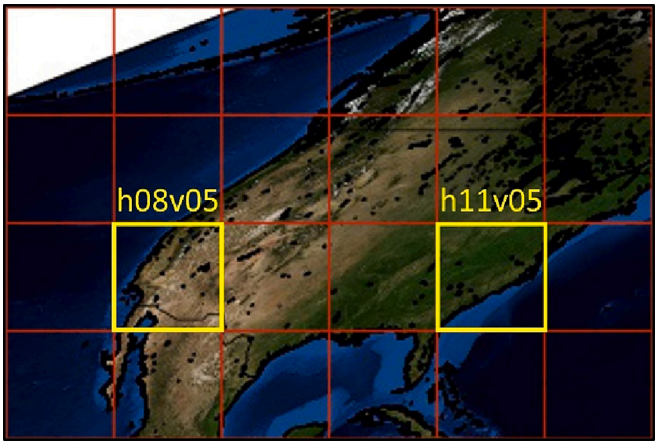

Fig. 6. Location of tiles H08V05 and H11V05 in map of North America in global sinusoidal projection.

4. MAIAC assessment of VIIRS calibration

We selected two MODIS/VIIRS 1200 × 1200 km^2 tiles, H11V05 in south-eastern USA with high forest, grassland and agricultural crops vegetation cover, and H08V05 partly covering states of California, Texas, and Arizona with high fraction of bright surface in semi-arid and arid climate zones. Location of tiles is shown in Fig. 6. Applying the developed VIIRS calibration, we processed 4 years of the common record period from 2018 to 2021. Below, we analyze agreement in MAIAC geophysical records from the three sensors including AOD, spectral surface reflectance and NDVI.

4.1. AOD comparison

Fig. 7 shows histograms of AOD difference between VIIRS and MODIS Aqua over land and water. The land comparison separates cases of low $AOD_{0.55} \leq 0.6$ (left) and high $AOD_{0.55} > 0.6$ (center). The water case includes all AODs over the in-land water and coastal ocean. The comparison is provided for the common green (0.55 μm) band and the blue band (B3 for MODIS and M2 for VIIRS). To harmonize MODIS and VIIRS data, we aggregated data to ~4 × 4 km^2 super-pixels, namely 4 × 4 pixels for MODIS and 5 × 5 pixels for VIIRS providing exact area match in 1200 km tiles. We used pairs with more than 70% coverage and time difference within ±15 min. This comparison shows an excellent agreement both over water and over land, in particular at "low AOD", with mean difference ~ 0.01 and residual mean squared difference (*rmsd*) ~0.04. This indicates a high accuracy of VIIRS-to-MODIS cross-calibration across the full spectrum, as MAIAC uses different sets of bands for aerosol retrieval over land (B3/M2, B4/M4 and B7/M11) and over water (B4/M4, B1/M5, B2/M7, B5/M8, B6/M10, B7/M11). It also sets a balanced starting point for atmospheric correction: MAIAC performs BRDF retrieval when $AOD_{0.47} \leq 0.6$ and reports spectral BRF at $AOD_{0.47} < 1.5$. At "High AOD" over land, the overall VIIRS-MODIS agreement remains good with *rmsd* ~ 0.1 and slight positive difference 0.01–0.04 in the Blue, expected as M2 is shorter than B3, and a small negative difference of ~ − 0.03 at 0.55 μm from an average $AOD_{0.55}$–0.82. Some of the difference may be explained by variations in coverage of super-pixels (within 70–100%), and smoke plume inhomogeneities arising from both overpass time difference and parallax effect from different view angles resulting in sensors' seeing different parts of the elevated smoke.

4.2. Surface reflectance

Contrary to the commonly used Lambertian approximation, MAIAC uses a BRDF-coupled radiative transfer model in atmospheric correction to retrieve surface reflectance (BRF) (Lyapustin et al., 2012, 2018, 2021). We start with comparing MAIAC surface reflectance between the two VIIRS sensors. To avoid difference in view geometry due to different orbits, we first normalize SR to a nadir view and local solar angle at 1:30 pm using BRDF model, thus creating "nadir BRDF-adjusted reflectance" (NBAR) in M-bands 1–5, 7, 8, 10–11, and I1-I3. As before, NBARs are aggregated to ~4 × 4 km^2. The daily average NBARs for super-pixels are used for comparison when they have 100% coverage and both sensors have data.

The results of VIIRS to VIIRS (VtoV) spectral NBAR comparison are shown in Fig. 8 as a combination of scatterplots and SNPP-N20 difference histograms with associated statistics. The the mean difference (*MD*) is generally negligible: the NBARs agree within ±0.002 with maximal *MD* of 0.003 in bands M3, M11, I3. The *rmsd* is about 0.008 in bright NIR-SWIR bands, and less than 0.004–0.006 in the visible. The exception is band M1 where larger *rmsd* = 0.007 is due to the "wings" nearly parallel to the *x*,*y*-axes. These outliers are created by the BRDF-normalization at high view zenith angles. They are most prominent at the shortest wavelength M1 where uncertainties of atmospheric correction and of the BRDF model are the highest. To illustrate the point, similar cross-sensor comparisons VIIRS M1 vs MODIS-A B8 NBAR are shown in the next Fig. 9 for a limited range of view zenith angles VZA < 35° which dramatically reduces such outliers.

A similar Fig. 9 presents VIIRS to MODIS-A (VtoM) NBAR comparison. Here, we excluded VIIRS observations at high view zenith angles above 62° approximately corresponding to the maximum MODIS VZA with account for the Earth curvature. MODIS and VIIRS RSRs have significant differences in the Blue (M2, M3 vs B3), Red (M5 vs B1), and SWIR (M10/I3 vs B6 and M11 vs B7) bands, while center wavelengths and RSRs for other bands are relatively close. In "matching" bands M4/B4 and M7/B2, the *MD* (0.000 and 0.002) and *rmsd* (0.005 and 0.008)

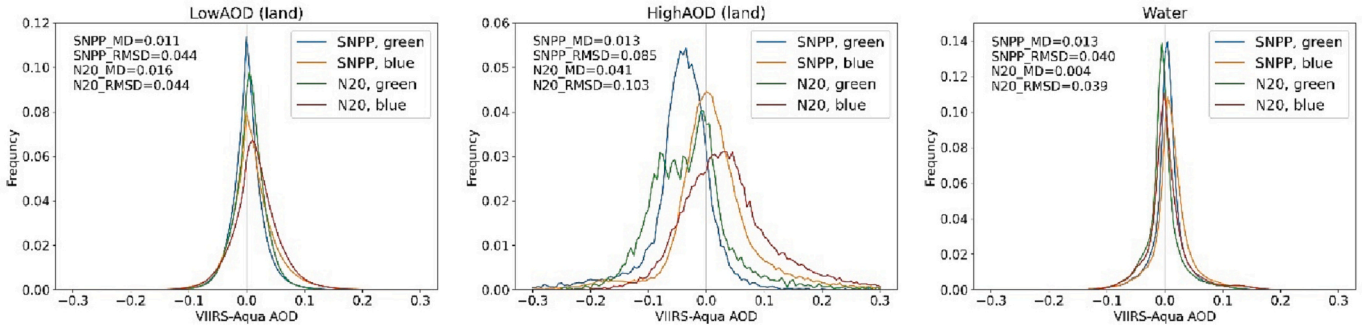

Fig. 7. AOD difference histogram (2018–2021) between VIIRS and MODIS-A over land and water. The land comparison separates cases of low $AOD_{0.55} \leq 0.6$ (left) and high $AOD_{0.55} > 0.6$ (center). The water case includes all AODs over the in-land water and ocean. The comparison is given for the common green (0.55 μm) and the blue band (B3 for MODIS and M2 for VIIRS). The *MD* and *rmsd* are provided for the Blue band (M2 for VIIRS and B3 for MODIS). (For interpretation of the references to colour in this figure legend, the reader is referred to the web version of this article.)

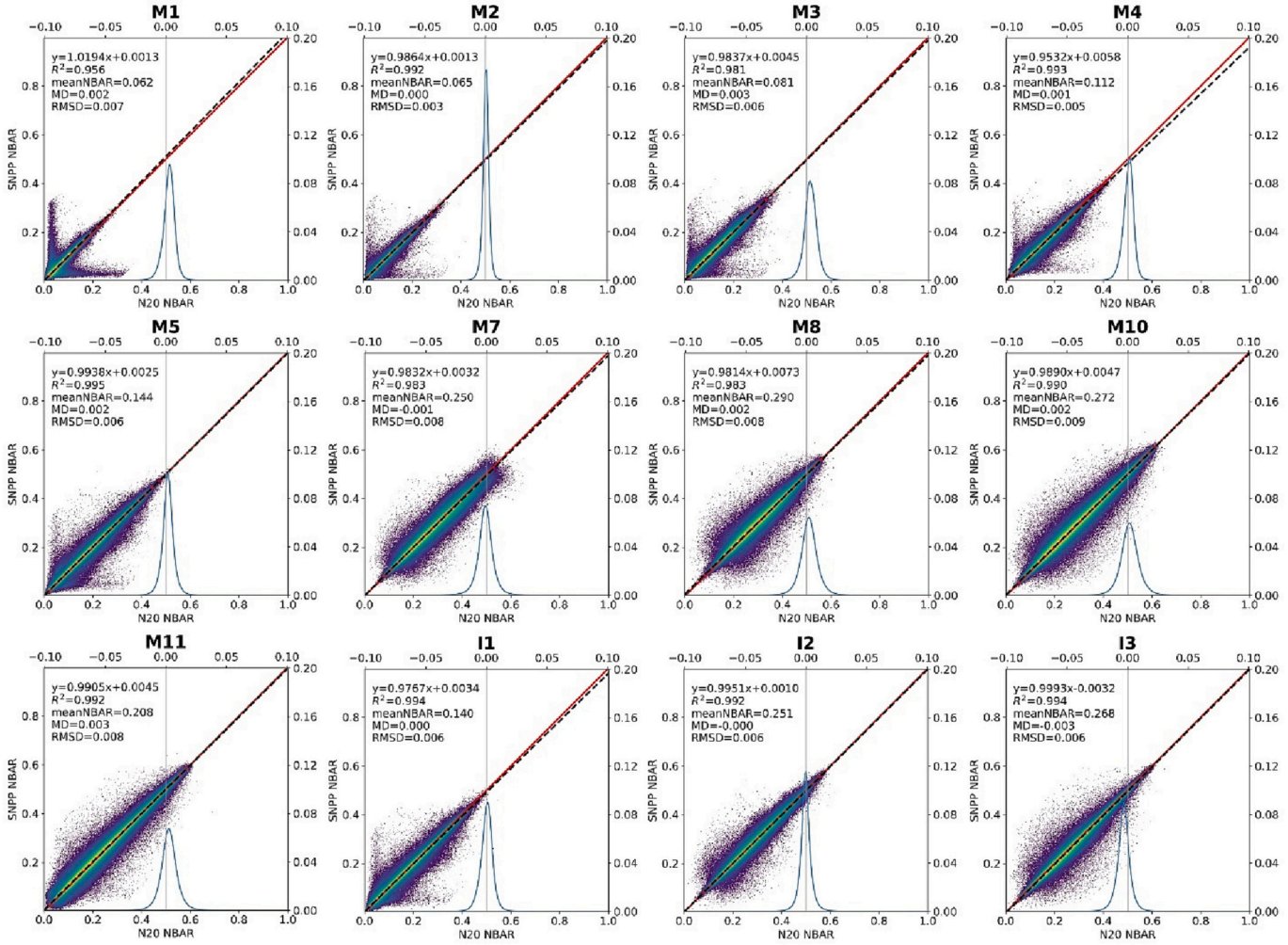

Fig. 8. A comparison of spectral NBARs between SNPP and NOAA 20 VIIRS. The X-axis for the histogram of NBAR difference is given on top and right for $NBAR_{Y\text{-}axis}$ – $NBAR_{X\text{-}axis}$ for each plot.

remain low and similar to the VtoV comparison. In NIR-SWIR region (M8/B5, M10/B6, M11/B7), the *MD* increases to within ±0.004 for N20 and − 0.002–0.006 for SNPP. The *rmsd* in these bands increases to 0.010–0.013 or ~ 20–50% respective to VtoV comparison. For the non-matching bands M2/B3, M3/B3, M5/B1, we see an expected pattern related to general SR increase with wavelength in this part of spectrum. Somewhat surprisingly to us, this rather large-scale comparison between M11 (2.25 μm) and B7 (2.13 μm) shows a much closer agreement than we expected. It should be mentioned, though, that 1) we excluded snow pixels where the difference is most significant, and 2) spectral mis-match is apparent at the level of individual pixels as histogram of difference for this channel is most asymmetric (non-Gaussian) among all compared bands. The VtoM comparison for both VIIRS sensors shows an *MD* within 0.002 and a nearly identical *rmsd* for the same band pairs.

In summary, the NBAR comparison shows very consistent VtoV and VtoM patterns for both SNPP and NOAA 20 indicating a good quality of performed calibration. The VtoM *rmsd* of 0.005–0.007 in the darker visible and of 0.008–0.013 in brighter NIR-SWIR bands can be considered as an uncertainty of continuity or transitioning of MODIS MAIAC surface reflectance record into the era of VIIRS observations.

4.3. Normalized difference vegetation index (NDVI)

Beginning with MODIS Collection 6.1, available since June 2023, and VIIRS Collection 2 (MAIAC re-processing to start in summer of 2023), the naturally gap-filled NDVI, spectral BRDF and snow fraction/snow grain size will be reported by MAIAC daily. MAIAC uses an assumption-free "natural gap-filling" meaning that the value (e.g., NDVI) remains in the memory for a given grid cell until updated with the latest cloud-free observations.

Fig. 10 (top) shows analysis for VIIRS $NDVI_M$ based on radiometric bands M5/M7. As with NBAR, NDVI is aggregated to ~4 × 4 km^2 super-pixels. MODIS NIR band B2 (0.856 μm) is slightly shorter than the NIR band of VIIRS sensors (0.861 μm and 0.867 μm for SNPP and N20) for both radiometric and imagery bands which are nearly identical, resulting in slightly lower MODIS NIR SR. The VIIRS radiometric Red band M5 is over 20 nm longer than the MODIS Red band B1 resulting in higher SR_{Red}. For these reasons, VIIRS $NDVI_M$ is slightly higher than MODIS NDVI at high NDVI over dense vegetation and is lower at low NDVI over bare soil/sand. This tendency is more apparent for NOAA 20 VIIRS. A similar though less pronounced pattern can be seen in comparison of the VIIRS SNPP vs N20 $NDVI_M$ due to similar RSR differences. The VtoV $NDVI_M$ has *rmsd* = 0.014, which increases to ~0.02 for VtoM comparison. We should mention that the $NDVI_M$ were computed from NBARs and represent geometrically normalized values. A comparison of standard $NDVI_M$ gives generally similar results but with 40–50% higher *rmsd*.

Fig. 10 (bottom) compares NDVIs based on the VIIRS imagery bands I1/I2 ($NDVI_I$). As center wavelength of the VIIRS imagery Red band (0.638 μm for SNPP and 0.643 μm for N20) is closer to that of MODIS-A (0.646 μm) in comparison to band M5 (~0.67 μm), we can expect a better agreement of $NDVI_I$ with MODIS-A NDVI. Indeed, VtoM

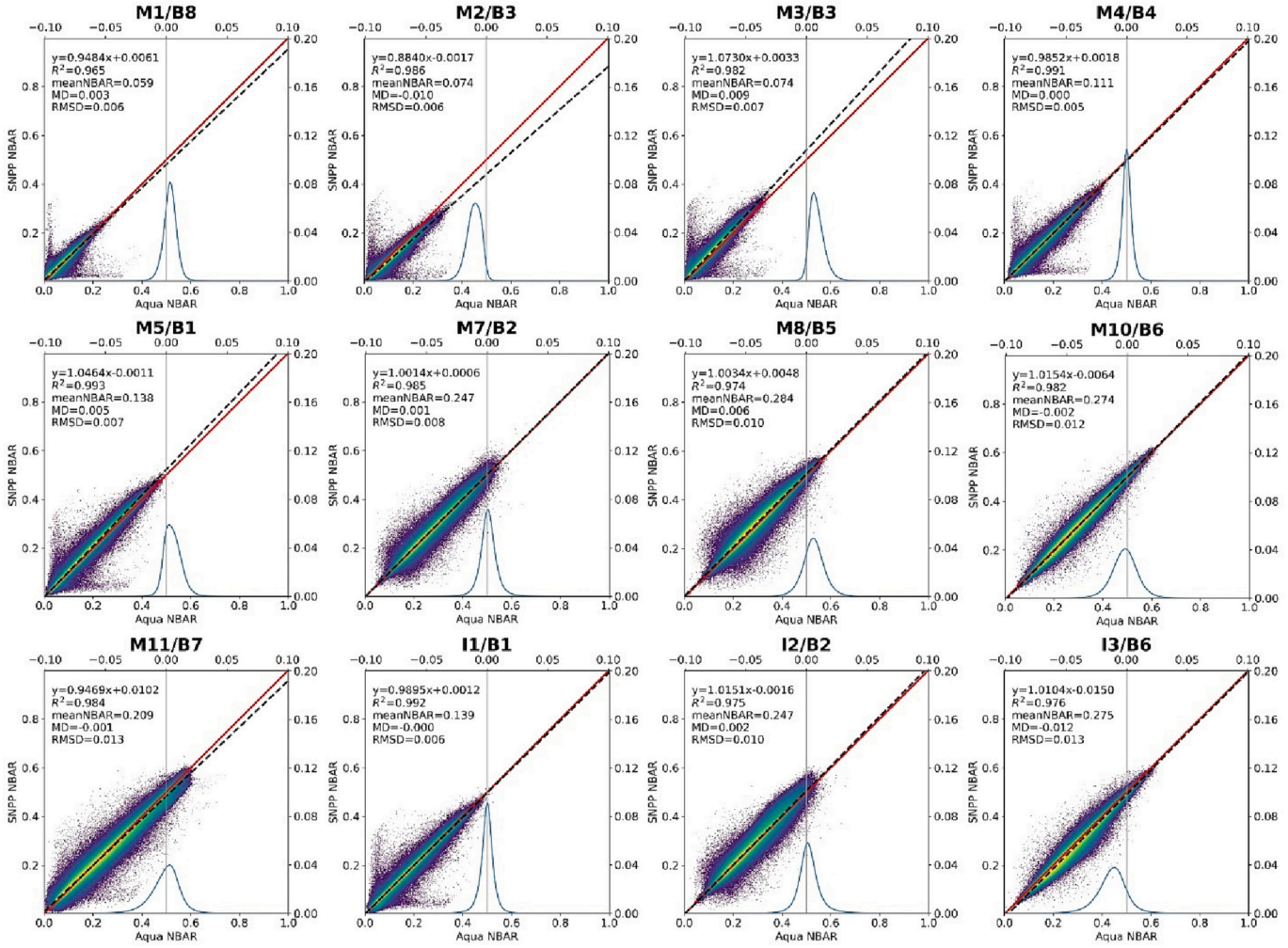

Fig. 9. A comparison of spectral NBARs between VIIRS SNPP and MODIS Aqua (top) and NOAA 20 VIIRS and MODIS Aqua (bottom). (For interpretation of the references to colour in this figure legend, the reader is referred to the web version of this article.)

comparison shows a better slope close to 1 and smaller MD. However, *rmsd* is larger in particular for VtoV $NDVI_I$ (0.021) vs $NDVI_M$ (0.014) comparison. The main contributor to higher *rmsd* is the bottom half of NDVI values where the distribution of $NDVI_I$ points around the 1:1 line is visually wider.

As satellite-based NDVI is one of important climate data records also widely used in different applications such as drought monitoring (e.g., Gu et al., 2007), crop yield predictions (e.g., Pittman et al., 2010) and others, it is important to understand the role of RSR differences in relationships displayed in Fig. 10. To this end, we employ several types of soil/sand (S) spectra and two types of vegetation (V) spectra (Kokaly et al., 2017) shown in Fig. 11. We use the band-integrated Red and NIR SR, and a linear mixing model to represent a variety of NDVI values. For each S—V combination, the soil fraction varies from 1 to 0. This oversimplified model to some extent represents S—V fractional variations with view zenith angle for moderately to sparsely vegetated surfaces where visible soil fraction is maximal at nadir and decreases with VZA approximately as cos(VZA).

The analogue of Fig. 10 generated from the described model is presented in Fig. 12 (left) where different lines correspond to different spectra of soil. Qualitatively, this simple analysis gives very similar statistical estimates to those obtained with MODIS-VIIRS satellite data in Fig. 10. For instance, the absolute value of $NDVI_I$ mean difference is lower than that for $NDVI_M$. The slope of regression is notably above 1 with negative *MD* for VtoM $NDVI_M$ comparisons, and slope is close to or below 1 with positive *MD* for $NDVI_I$ comparison. In VtoV comparison, the slope of SNPP vs N20 regression is less than 1, and it is lower for $NDVI_I$ in agreement with Fig. 10.

While reproducing (most of) statistical estimates of satellite observations, our model lacks realism in visual comparison and needs to be augmented by the random noise of BRDF-normalization. This noise can be mainly associated with imperfect BRDF retrievals from limited angular sampling and with limited accuracy of the BRDF model itself. We assumed the maximal random error of BRDF-normalization as 3% of NBAR value in the Red and 1% in the NIR. These values are realistic given that the MODIS/VIIRS surface reflectance range of variability with VZA can be as high as 30–100% in the Red and 10–30% in the NIR. The result of adding an independent random noise from zero to the maximum value to every NDVI point is shown in Fig. 12 (right). Not surprisingly, it increases *rmsd* but has little effect on the *MD*.

The selected level of noise allows us to match the observed *rmsd* ~ 0.02 for the $NDVI_I$, however it overestimates *rmsd* for the $NDVI_M$ (~0.03 vs ~0.02 for VtoM comparison). Indeed, we used the 750 m M5/M7 BRDF models for angular normalization of both M and I-bands. Over heterogeneous surfaces, it creates an additional noise in 375 m $NDVI_I$, and since we matched the $NDVI_I$ *rmsd*, a proportionally lower noise can be justifiably used to match *rmsd* for $NDVI_M$.

In summary, a simple soil-vegetation linear mixture model, which

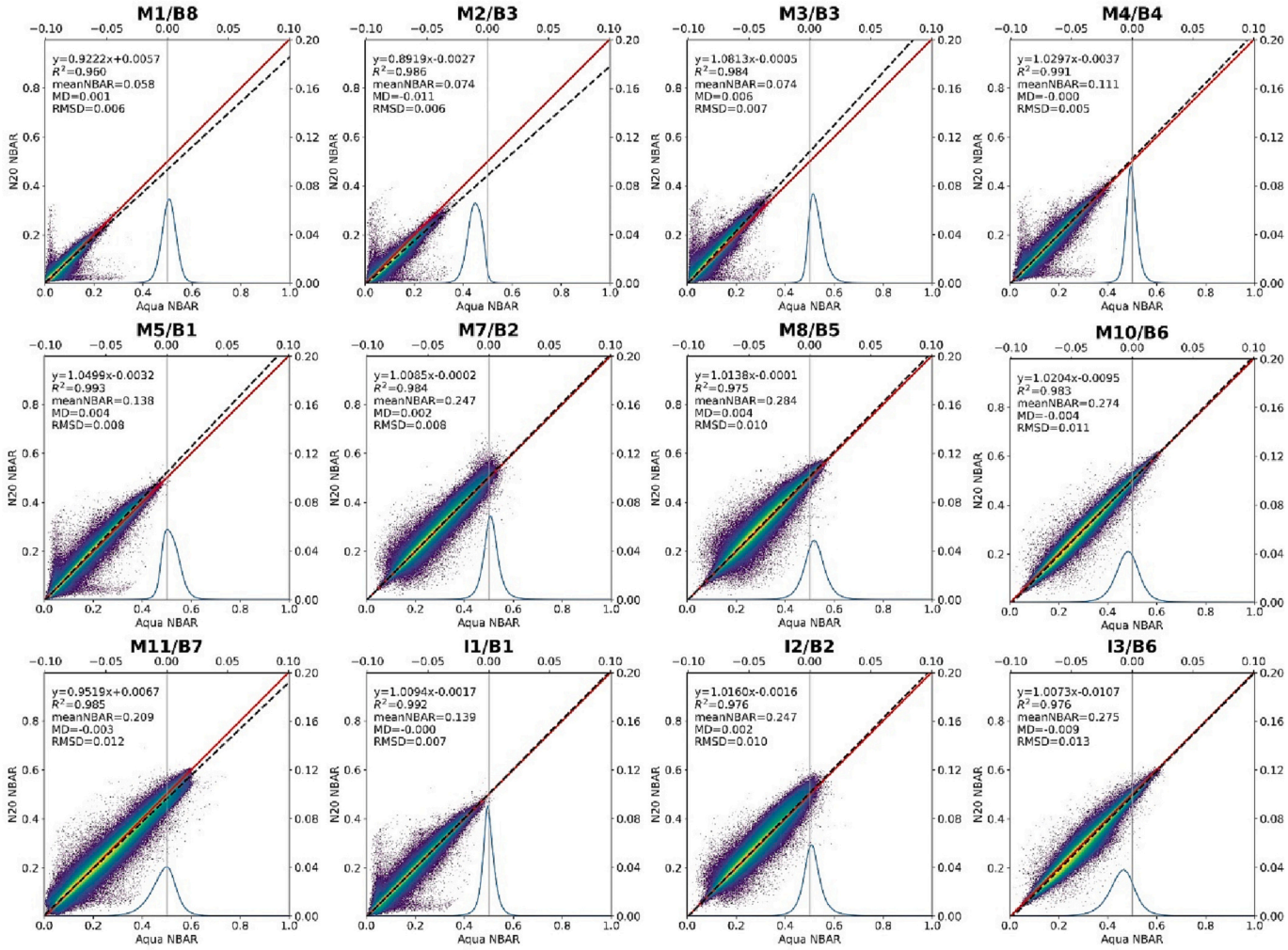

Fig. 9. (*continued*).

accounts for RSR differences, with added noise of BRDF-normalization allows us to approximate and explain the observed statistical relationships among NDVI from MODIS-A and $NDVI_M$/ $NDVI_I$ from VIIRS SNPP and NOAA 20. This discussion shows that with applied calibration MODIS and VIIRS NDVIs will match well for dense closed canopies. The RSR differences, mainly transpiring at low NDVI, can be decoupled by separating the non-photosynthetic signal through finding the vegetation fraction at nadir. With developed calibration and without any adjustments, the MODIS – VIIRS NDVIs agree within *rmsd* ~ 0.02 and an average *MD* -0.01 for $NDVI_M$ and 0.003 for $NDVI_I$. A different way to achieve MODIS-VIIRS continuity of NDVI, albeit with higher uncertainty, was suggested by Skakun et al. (2018) who modeled VIIRS Red and NIR SR as a linear combination of MODIS Red and NIR SR with weights defined separately for every pixel.

5. Conclusions

In this work, we applied MAIAC-based vicarious calibration technique over Libya-4 desert site to perform calibration analysis of VIIRS on the SNPP and NOAA-20 satellites. For both VIIRS sensors, we characterized the residual linear calibration trend and cross-calibrated both sensors to MODIS Aqua regarded here as a calibration standard. RSR differences were accounted for using DESIS hyperspectral LER data. Because DESIS calibration was found very close to that of MODIS Aqua, the developed SBAFs should help achieve a better VIIRS calibration accuracy as compared to the use of standard SBAFs based on SCIAMACHY data. We compared the cross-calibration results to those obtained by other teams using a variety of techniques and found general agreement in the spectral patterns and magnitudes of derived correction factors. A general agreement within ~1% between MAIAC-based results with dedicated analyses of MCST/VCST and CERES-IGCG calibration teams ensures reliability of VIIRS calibration for the science processing.

Analysis of MAIAC geophysical products with the newly developed calibration shows a very good consistency and continuity of MAIAC aerosol, surface reflectance and NDVI records between MODIS and VIIRS. Over water and at $AOD_{0.55} < 0.6$ over land, all three sensors agree on AOD with *MD* less than 0.01 and *rmsd* ~ 0.04. Spectral NBARs, obtained from surface reflectance normalized to nadir view and local SZA at 1:30 pm, agree within *rmsd* of 0.003–0.005 in the visible and 0.01–0.012 at longer wavelengths. The residual differences in the magnitude of SR are well explained by the RSR differences. Finally, difference in NDVI is characterized by *rmsd* ~ 0.02 and *MD* less than 0.003 for $NDVI_I$ based on VIIRS imagery bands and 0.01 for $NDVI_M$ based on VIIRS radiometric bands. The observed NDVI difference patterns can be well explained by a simple soil-vegetation linear mixture model with RSR-integration and added noise of BRDF normalization.

Accurate calibration to ensure consistency and continuity of geophysical products of the atmosphere, land and ocean disciplines within the mission period and among different sensors, supported by periodic re-processing with latest calibration, is a major requirement of the Earth System data records in both applied research and climate studies. It has been systematically implemented in the NASA MODIS

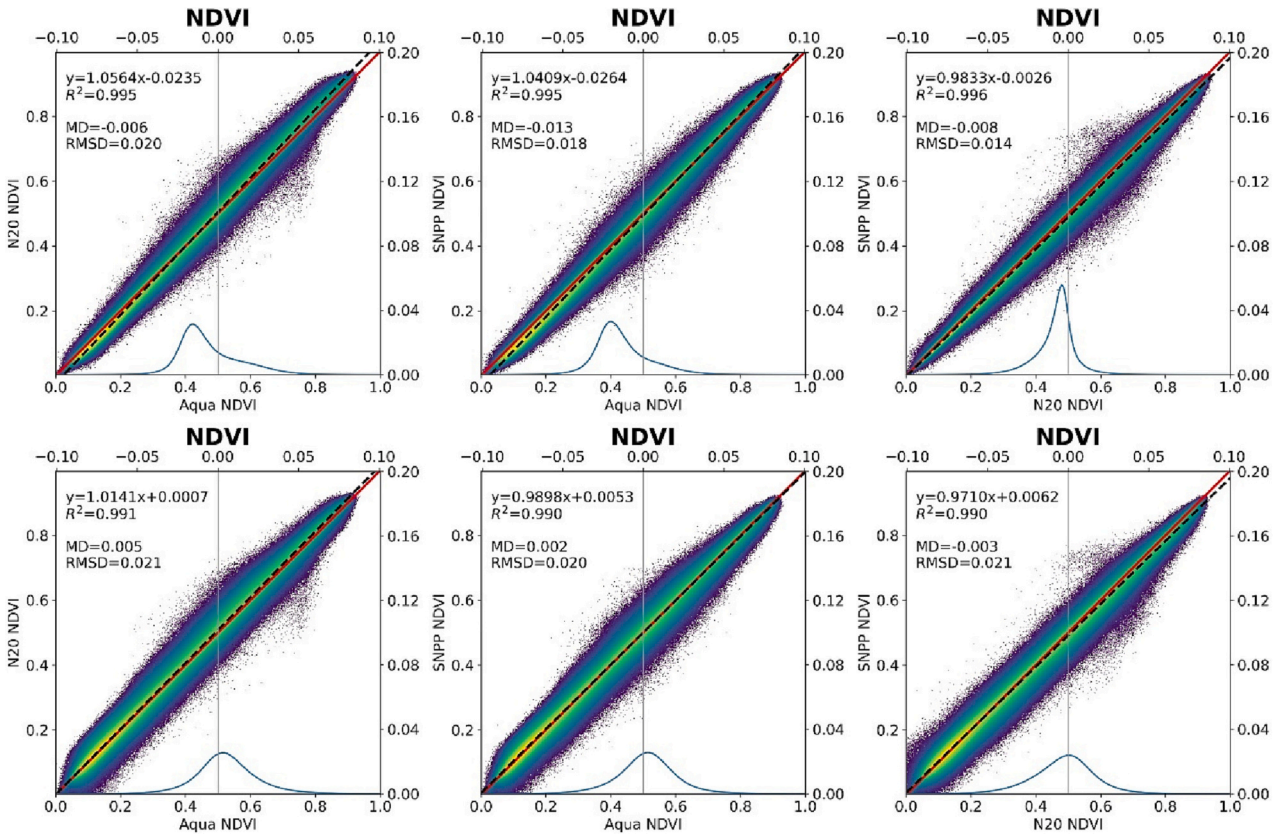

Fig. 10. A comparison of NDVI among VIIRS SNPP, VIIRS NOAA 20 and MODIS Aqua based on radiometric VIIRS bands M5/M7 (top) and imagery bands I1/I2 (bottom). The X-axis for the histogram of NDVI difference is given on top and right for $NDVI_{Y\text{-}axis} - NDVI_{X\text{-}axis}$ for each plot. (For interpretation of the references to colour in this figure legend, the reader is referred to the web version of this article.)

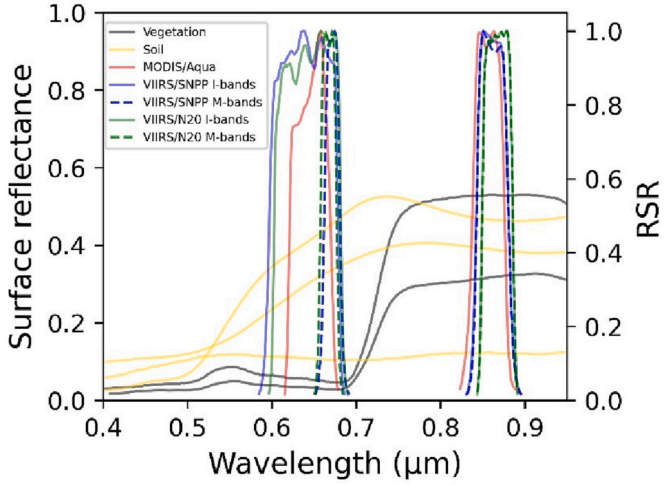

Fig. 11. Typical soil and vegetation spectra (https://crustal.usgs.gov/speclab/SpLib07b_Spectrum.php) and RSRs for the Red and NIR bands of MODIS-Aqua and VIIRS SNPP and NOAA 20. (For interpretation of the references to colour in this figure legend, the reader is referred to the web version of this article.)

operational processing currently in Collection 6.1 and continues in the NASA VIIRS processing. The NASA VIIRS Collection 2 land discipline re-processing is ongoing, and MAIAC VIIRS Collection 2 re-processing with described residual calibration, supporting the main effort by VCST, will begin in summer of 2023.

The developed approach is generic and will be applied to similarly align the VIIRS NOAA 21 which recently became operational.

CRediT authorship contribution statement

Alexei Lyapustin: Conceptualization, Methodology, Supervision, Writing – original draft. **Yujie Wang:** Software, Investigation, Visualization. **Myungje Choi:** Software, Investigation, Visualization. **Xiaoxiong Xiong:** Methodology, Software, Data curation, Writing – review & editing. **Amit Angal:** Methodology, Software, Data curation, Writing – review & editing. **Aisheng Wu:** Methodology, Software, Data curation, Writing – review & editing. **David R. Doelling:** Methodology, Software, Data curation, Writing – review & editing. **Rajendra Bhatt:** Methodology, Software, Data curation, Writing – review & editing. **Sujung Go:** Software, Investigation, Visualization. **Sergey Korkin:** Software, Investigation, Visualization. **Bryan Franz:** Writing – review & editing. **Gerhardt Meister:** Writing – review & editing. **Andrew M. Sayer:** Methodology, Software, Data curation, Writing – review & editing. **Miguel Roman:** Supervision, Writing – review & editing. **Robert E. Holz:** Writing – review & editing. **Kerry Meyer:** Methodology, Software, Data curation, Writing – review & editing. **James Gleason:** Supervision, Writing – review & editing. **Robert Levy:** Writing – review & editing.

Declaration of Competing Interest

The authors declare that they have no known competing financial interests or personal relationships that could have appeared to influence the work reported in this paper.

Data availability

Data will be made available on request.

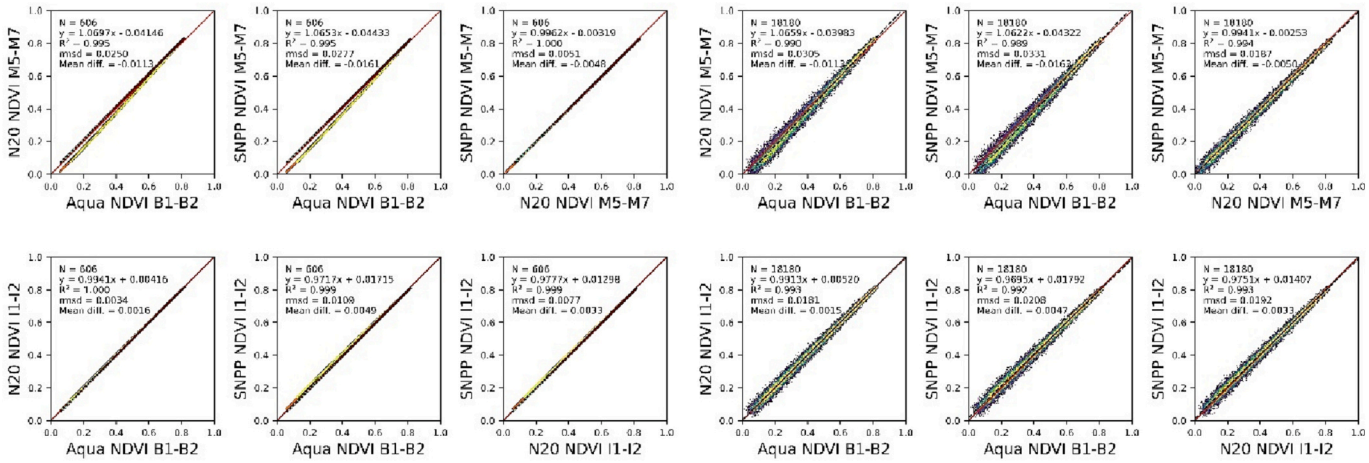

Fig. 12. A comparison of NDVI, analogous to Fig. 10, based on the soil – vegetation linear mixture analysis with RSR-integration (left) and added noise of BRDF-normalization (right).

Acknowledgements

The work of A. Lyapustin, Y. Wang, S Korkin, S. Go and M. Choi were supported by the NASA MODIS maintenance program and NASA NNH20ZDA001N-SNPPSP funding (HQ program manager Dr. M Falkowski). We acknowledge support of the NASA Supercomputing Center for Climate Simulations (NCCS) that enabled this analysis and members of the CERES-IGCG at NASA LaRC (Benjamin Scarino, Arun Gopalan, Conor Haney, and Prathana Khakurel) for their support with processing MODIS and VIIRS intercalibration data.

References

Alonso, K., Bachmann, M., Burch, K., Carmona, E., Cerra, D., de los Reyes, R., Dietrich, D., Heiden, U., Hölderlin, A., Ickes, J., Knodt, U., Krutz, D., Lester, H., Müller, R., Pagnutti, M., Reinartz, P., Richter, R., Ryan, R., Sebastian, I., Tegler, M., 2019. Data products, quality and validation of the DLR earth sensing imaging spectrometer (DESIS). Sensors (Switzerland) 19 (20), 1–44. https://doi.org/10.3390/s19204471.

Angal, A., Geng, X., Xiong, X., Twedt, K., Wu, A., Link, D., Aldoretta, E., 2020. On-orbit calibration of Terra MODIS VIS bands using polarization-corrected desert observations. IEEE Trans. Geosci. Remote Sens. 12, 1915.

Bhatt, R., Doelling, D.R., Angal, A., Xiong, X., Haney, C.O., Scarino, B.R., Wu, A., Gopalan, A., 2020. Response versus scan-angle assessment of MODIS reflective solar bands in collection 6.1 calibration. IEEE Trans. Geosci. Remote Sens. 58 (4), 2276–2289. https://doi.org/10.1109/TGRS.2019.2946963.

Bhatt, R., Doelling, D.R., Coddington, O., Scarino, B., Gopalan, A., Haney, C., 2021. Quantifying the impact of solar spectra on the inter-calibration of satellite instruments. Remote Sens. 13 (8), 1438. https://doi.org/10.3390/rs13081438.

Bovensmann, H., Burrows, J.P., Buchwitz, M., Frerick, J., Noël, S., Rozanov, V.V., Chance, K.V., Goede, A.P.H., 1999. SCIAMACHY: Mission objectives and measurement modes. J. Atmos. Sci. 56 (2), 127–150.

Cao, C., Weinreb, M., Xu, H., 2004. Predicting simultaneous nadir overpasses among polar-orbiting meteorological satellites for intersatellite calibration of radiometers. J. Atmos. Ocean. Technol. 21, 537–542.

Choi, T., Cao, C., Blonski, S., Wang, W., Uprety, S., Shao, X., 2020. NOAA-20 VIIRS reflective solar band postlaunch calibration updates two years in-orbit. IEEE Trans. Geosci. Remote Sens. 58 (11), 7633–7642. https://doi.org/10.1109/TGRS.2020.2982764.

Chu, M., Sun, J., Wang, M., 2018. Performance evaluation of on-orbit calibration of SNPP VIIRS reflective solar bands via Intersensor comparison with aqua MODIS. J. Atmos. Ocean. Technol. 35, 385–403. https://doi.org/10.1175/JTECH-D-17-0008.1.

Coddington, O., Lean, J.L., Pilewskie, P., Snow, M., Lindholm, D., 2016. A solar irradiance climate data record. Bull. Am. Meteorol. Soc. 97 (7), 1265–1282. https://doi.org/10.1175/BAMS-D-14-00265.1.

Doelling, D.R., Morstad, D., Bhatt, R., Scarino, B., 2011. Algorithm theoretical basis document (ATBD) for deep convective cloud (DCC) technique of calibrating GEO sensors with aqua-MODIS for GSICS., 10 pp. GSICS Available: http://gsics.nesdis.noaa.gov/pub/Development/AtbdCentral/GSICS_ATBD_DCC_NASA_2011_09.pdf.

Doelling, D.R., Morstad, D., Scarino, B.R., Bhatt, R., Gopalan, A., 2013. The characterization of deep convective clouds as an invariant calibration target and as a visible calibration technique. IEEE Trans. Geosci. Remote Sens. 51 (3), 1147–1159. https://doi.org/10.1109/TGRS.2012.2225066.

Doelling, D.R., Wu, A., Xiong, X., Scarino, B.R., Bhatt, R., Haney, C.O., Morstad, D., Gopalan, A., 2015. The radiometric stability and scaling of collection 6 Terra- and Aqua-MODIS VIS, NIR, and SWIR spectral bands. IEEE Trans. Geosci. Remote Sens. 53 (8), 4520–4535.

Doelling, David R., Haney, Conor, Bhatt, Rajendra, Scarino, Benjamin, Gopalan, Arun, 2022a. Daily monitoring algorithms to detect geostationary imager visible radiance anomalies. J. Appl. Remote. Sens. 16 (1), 014502 https://doi.org/10.1117/1.JRS.16.014502.

Doelling, David R., Khakurel, Prathana, Haney, Conor, Bhatt, Rajendra, Scarino, Benjamin R., Gopalan, Arun, 2022b. Additional characterization of Libya-4 in support of post-launch vicarious calibration of satellite imagers. In: Proc. SPIE 12232, Earth Observing Systems XXVII, p. 1223219 (30 September 2022). https://doi.org/10.1117/12.2633118.

Eplee, R., Turpie, K., Meister, G., Patt, F., Franz, B., Bailey, S., 2015. On-orbit calibration of the Suomi National Polar-Orbiting Partnership Visible Infrared Imaging Radiometer Suite for ocean color applications. Appl. Opt. 54, 1984–2006.

Esaias, E., Abbott, M., Barton, I., Brown, O., Campbell, J., Carder, K., Clark, D., Evans, R., Hoge, F., Gordon, H., et al., 1998. An overview of MODIS capabilities for ocean science observations. IEEE Trans. Geosci. Remote Sens. 36, 1250–1265.

Gu, Y., Brown, J.F., Verdin, J.P., Wardlow, B., 2007. A five year analysis of MODIS NDVI and NDWI for grassland drought assessment over the central Great Plains of the United States. Geophys. Res. Lett. 34 (6), L06407. https://doi.org/10.1029/2006GL029127.

Haney, C., Doelling, D.R., Su, W., Bhatt, R., Gopalan, A., Scarino, B., 2022. Radiometric stability assessment of the DSCOVR EPIC visible bands using MODIS, VIIRS, and invariant targets as independent references. Front. Remote Sens. 2, 765913 https://doi.org/10.3389/frsen.2021.765913.

Justice, C., Vermote, E., Townshend, J., Defries, R., Roy, D., Hall, D., Salomonson, V., Privette, J., Riggs, G., Strahler, A., et al., 1998. The moderate resolution imaging spectroradiometer (MODIS): land remote sensing for global change research. IEEE Trans. Geosci. Remote Sens. 36, 1228–1249.

King, M., Menzel, P., Kaufman, Y., Tanre, D., Gao, B., Platnick, S., Ackerman, S., Remer, L., Pincus, R., Hubanks, P., 2003. Cloud and aerosol properties, precipitable water, and profiles of temperature and water vapor from MODIS. IEEE Trans. Geosci. Remote Sens. 41, 442–458.

Kokaly, R.F., Clark, R.N., Swayze, G.A., Livo, K.E., Hoefen, T.M., Pearson, N.C., Wise, R. A., Benzel, W.M., Lowers, H.A., Driscoll, R.L., Klein, A.J., 2017. USGS spectral library version 7: U.S. Geol. Surv. Data Ser. 1035 https://doi.org/10.3133/ds1035, 61 p.

Krutz, D., Müller, R., Knodt, U., Günther, B., Walter, I., Sebastian, I., Säuberlich, T., Reulke, R., Carmona, E., Eckardt, A., Venus, H., Fischer, C., Zender, B., Arloth, S., Lieder, M., Neidhardt, M., Grote, U., Schrandt, F., Gelmi, S., Wojtkowiak, A., 2019. The instrument design of the DLR earth sensing imaging spectrometer (DESIS). Sensors (Switzerland) 19 (7), 1–16. https://doi.org/10.3390/s19071622.

Kwiatkowska, E.J., Franz, B.A., Meister, G., McClain, C.R., Xiong, X., 2008. Cross calibration of ocean-color bands from moderate resolution imaging Spectroradiometer on Terra platform. Appl. Opt. 47 (36), 6796–6810.

Lei, N., Xiong, X., Guenther, B., 2015. Modeling the detector radiometric gains of the Suomi NPP VIIRS reflective solar bands. IEEE Trans. Geosci. Remote Sens. 53 (3), 1565–1573. https://doi.org/10.1109/TGRS.2014.2345481.

Lucht, W., Schaaf, C.B., Strahler, A.H., 2000. An algorithm for the retrieval of albedo from space using semiempirical BRDF models. IEEE Trans. Geosci. Remote Sens. 38, 977–998.

Lyapustin, A.I., Wang, Y., Laszlo, I., Hilker, T., Hall, F., Sellers, P., Tucker, J., Korkin, S., 2012. Multi-angle implementation of atmospheric correction for MODIS (MAIAC): 3. Atmospheric correction. Remote Sens. Environ. 127, 385–393. https://doi.org/10.1016/j.rse.2012.09.002.

Lyapustin, A., Wang, Y., Xiong, X., Meister, G., Platnick, S., Levy, R., Franz, B., Korkin, S., Hilker, T., Tucker, J., Hall, F., Sellers, P., Wu, A., Angal, A., 2014. Scientific impact of MODIS C5 calibration degradation and C6+ improvements. Atmos. Meas. Tech. 7 (12), 4353–4365. https://doi.org/10.5194/amt-7-4353-2014.

Lyapustin, A., Wang, Y., Korkin, S., Huang, D., 2018. MODIS collection 6 MAIAC algorithm. Atmos. Meas. Tech. 11, 5741–5765. https://doi.org/10.5194/amt-11-5741-2018.

Lyapustin, A., Zhao, F., Wang, Y., 2021. A comparison of multi-angle implementation of atmospheric correction and MOD09 daily surface reflectance products from MODIS. Front. Remote Sens. 2, 712093 https://doi.org/10.3389/frsen.2021.712093.

Meister, G., Franz, B., Kwiatkowska, E., McClain, C., 2012. Corrections to the calibration of MODIS Aqua Ocean color bands derived from SeaWiFS data. IEEE Trans. Geosci. Remote Sens. 50 (1), 310–319. https://doi.org/10.1109/TGRS.2011.2160552.

Meyer, K., Platnick, S., Holz, R., Dutcher, S., Quinn, G., Nagle, F., 2020. Derivation of shortwave radiometric adjustments for SNPP and NOAA-20 VIIRS for the NASA MODIS-VIIRS continuity cloud products. Remote Sens. 12, 4096. https://doi.org/10.3390/rs12244096.

Mu, Q., Wu, A., Xiong, X., Doelling, D.R., Angal, A., Chang, T., Bhatt, R., 2017. Optimization of a deep convective cloud technique in evaluating the long-term radiometric stability of MODIS reflective solar bands. Remote Sens. 9 (6) issue 535.

Mu, Q., Wu, A., Xiong, X., Angal, A., 2020. Assessment of SNPP VIIRS RSB detector-to-detector differences using deep convective clouds and deserts. J. Appl. Remote. Sens. 14 (1), 1. https://doi.org/10.1117/1.JRS.14.018503.

Pittman, K., Hansen, M.C., Becker-Reshef, I., Potapov, P.V., Justice, C.O., 2010. Estimating global cropland extent with multi-year MODIS data. Remote Sens. 2 (7), 1844–1863. https://doi.org/10.3390/rs2071844.

Roujean, J.-L., Leroy, M., Deschamps, P.-Y., 1992. A bidirectional reflectance model of the Earth's surface for the correction of remote sensing data. J. Geophys. Res. 97 (D18), 20455. https://doi.org/10.1029/92JD01411.

Salomonson, V., Barnes, W., Maymon, P., Montgomery, H., Ostrow, H., 1989. MODIS: advanced facility instrument for studies of the earth as a system. IEEE Trans. Geosci. Remote Sens. 27, 145–153.

Sayer, A.M., Hsu, N.C., Bettenhausen, C., Holz, R.E., Lee, J., Quinn, G., Veglio, P., 2017. Cross-calibration of S-NPP VIIRS moderate resolution reflective solar bands against MODIS aqua over dark water scenes. Atmos. Meas. Tech. 10 (4), 1425–1444. https://doi.org/10.5194/amt-10-1425-2017.

Scarino, B.R., Doelling, D.R., Minnis, P., Gopalan, A., Chee, T., Bhatt, R., Lukashin, C., Haney, C., 2016. A web-based tool for calculating spectral band difference adjustment factors derived from SCIAMACHY hyperspectral data. IEEE Trans. Geosci. Remote Sens. 54 (5), 2529–2542.

Skakun, S., Justice, C.O., Vermote, E., Roger, J.-C., 2018. Transitioning from MODIS to VIIRS: an analysis of inter-consistency of NDVI data sets for agricultural monitoring. Int. J. Remote Sens. 39 (4), 971–992. https://doi.org/10.1080/01431161.2017.1395970.

Sun, J., Xiong, X., Angal, A., Chen, H., Wu, A., Geng, X., 2014. Time-dependent response versus scan angle for MODIS reflective solar bands. IEEE Trans. Geosci. Remote Sens. 52, 3159–3174.

Tilstra, L.G., Tuinder, O.N.E., Wang, P., Stammes, P., 2017. Surface reflectivity climatologies from UV to NIR determined from earth observations by GOME-2 and SCIAMACHY. J. Geophys. Res. 122 (7), 4084–4111. https://doi.org/10.1002/2016JD025940.

Twedt, K., Lei, N., Xiong, X., Angal, A., Li, S., Chang, T., Sun, J., 2022. On-orbit calibration and performance of NOAA-20 VIIRS reflective solar bands. IEEE Trans. Geosci. Remote Sens. 60, 1–13. https://doi.org/10.1109/TGRS.2021.3108970.

Uprety, S., Cao, C., 2015. Suomi NPP VIIRS reflective solar band on-orbit radiometric stability and accuracy assessment using desert and Antarctica dome C sites. Remote Sens. Environ. 166, 106–115.

Wu, A., Xiong, X., Doelling, D.R., Morstad, D., Angal, A., Bhatt, R., 2012. Characterization of Terra and Aqua MODIS VIS, NIR, and SWIR spectral Bands' calibration stability. IEEE Trans. Geosci. Remote Sens. 51 (7), 4330–4338.

Wu, A., Mu, Q., Angal, A., Xiong, X., 2020. Assessment of MODIS and VIIRS calibration consistency for reflective solar bands calibration using vicarious approaches. In: Proc. SPIE 11530, Sensors, Systems, and Next-Generation Satellites XXIV, p. 1153018 (20 September 2020). https://doi.org/10.1117/12.2573022.

Wu, A., Xiong, X., Bhatt, R., Haney, C., Doelling, D.R., Angal, A., Mu, Q., 2022. An assessment of SNPP and NOAA20 VIIRS RSB calibration performance in NASA SIPS reprocessed Collection-2 L1B data products. Remote Sens. 14, 4134. https://doi.org/10.3390/rs14174134.

Xiong, X., Chiang, K., Esposito, J., Guenther, B., Barnes, W.L., 2003. MODIS On-orbit Calibration and Characterization. Metrologia 40, 89–92. https://doi.org/10.1088/0026-1394/40/1/320.

Xiong, X., Angal, A., Chang, T., Chiang, K., Lei, N., Li, Y., Sun, J., Twedt, K., Wu, A., 2020. MODIS and VIIRS calibration and characterization in support of producing long-term high-quality data products. Remote Sens. 12, 3167. https://doi.org/10.3390/rs12193167.

Zhou, L., Divakarla, M., Liu, X., Layns, A., Goldberg, M., 2019. An overview of the science performances and calibration/validation of joint polar satellite system operational products. Remote Sens. 11, 698. https://doi.org/10.3390/rs11060698.